Atomic radical abatement of organic impurities from electron beam deposited metallic structures

Joshua D. Wnuk, Justin M. Gorham, and Samantha G. Rosenberg
Department of Chemistry, Johns Hopkins University, Baltimore, Maryland 21218

Theodore E. Madey[a)]
Department of Physics and Astronomy and Laboratory for Surface Modification, Rutgers, The State University of New Jersey, Piscataway, New Jersey 08854-8019

Cornelis W. Hagen
Faculty of Applied Sciences, Delft University of Technology, Lorentzweg 1, 2628CJ Delft, The Netherlands

D. Howard Fairbrother[b)]
Department of Chemistry, Johns Hopkins University, Baltimore, Maryland 21218

(Received 3 November 2009; accepted 8 March 2010; published 29 April 2010)

Focused electron beam induced processing (FEBIP) of volatile organometallic precursors has become an effective and versatile method of fabricating metal-containing nanostructures. However, the electron stimulated decomposition process responsible for the growth of these nanostructures traps much of the organic content from the precursor's ligand architecture, resulting in deposits composed of metal atoms embedded in an organic matrix. To improve the metallic properties of FEBIP structures, the metal content must be improved. Toward this goal, the authors have studied the effect of atomic hydrogen (AH) and atomic oxygen (AO) on gold-containing deposits formed from the electron stimulated decomposition of the FEBIP precursor, dimethyl-(acetylacetonate) gold(III), $Au^{III}(acac)Me_2$. The effect of AH and AO on nanometer thick gold-containing deposits was probed at room temperature using a combination of x-ray photoelectron spectroscopy (XPS), scanning Auger electron spectroscopy, and atomic force microscopy (AFM). XPS revealed that deposits formed by electron irradiation of $Au^{III}(acac)Me_2$ are only ≈10% gold, with ≈80% carbon and ≈10% oxygen. By exposing deposits to AH, all of the oxygen atoms and the majority of the carbon atoms were removed, ultimately producing a deposit composed of ≈75% gold and ≈25% carbon. In contrast, all of the carbon could be etched by exposing deposits to AO, although some gold atoms were also oxidized. However, oxygen was rapidly removed from these gold oxide species by subsequent exposure to AH, leaving behind purely metallic gold. AFM analysis revealed that during purification, removal of the organic contaminants was accompanied by a decrease in particle size, consistent with the idea that the radical treatment of the electron beam deposits produced close packed, gold particles. The results suggest that pure metallic structures can be formed by exposing metal-containing FEBIP deposits to a sequence of AO followed by AH. © *2010 American Vacuum Society.* [DOI: 10.1116/1.3378142]

I. INTRODUCTION

Fabrication of nanometer scale objects using focused electron beam induced processing (FEBIP) has recently been recognized as a potential addition to the suite of next-generation nanofabrication tools, such as electron beam lithography. FEBIP is a direct-write deposition technique where growth is initiated by a high energy and focused electron beam incident upon a substrate under low pressure conditions in the presence of a suitable gas-phase precursor molecule.[1–3] Nonvolatile products generated by electron induced decomposition of the precursor become the foundation for vertical nanostructure growth while repositioning of either the electron beam or the substrate results in horizontal deposition. In this way, two- and three-dimensional nanoscale structures can be deposited at a resolution of ≈1.0 nm.[4,5] Current applications of FEBIP include photolithographic mask repair and the production of high aspect ratio scanning probe tips.[6–14] Future applications may include the fabrication of nanoelectronic components.[15–21]

Various metal-containing nanostructures, for example, platinum, nickel, tungsten, iron and copper, have been successfully fabricated using FEBIP.[22–26] The deposition of gold nanostructures is of particular interest due to their potential applications as active components in sensors, field emitter devices, quantum optical systems, and nanoelectronic devices.[27–30] For gold deposition, the most common organometallic precursors are dimethyl-(hexafluoroacetylacetonate) gold(III) $[Au^{III}(hfac)Me_2]$, dimethyl-(trifluoroacetylacetonate) gold(III) $[Au^{III}(tfac)Me_2]$, and dimethyl-(acetylacetonate) gold(III) $[Au^{III}(acac)Me_2]$.[2]

a)Deceased.
b)Author to whom correspondence should be addressed; electronic mail: howardf@jhu.edu

Currently, the technological value of nanoscale, metallic structures fabricated using FEBIP is diminished by the entrapment of nonmetallic atoms associated with the precursor's ligand architecture during the deposition process. This results in deposits with high organic content (mostly carbon) and correspondingly poor metallic character.[31] Strategies to increase the purity of metal-containing nanostructures were recently the topic of a review by Botman *et al.*,[32] discussing the use of variable electron beam parameters as well as *in situ* and *ex situ* annealing and reactive gas treatments. For example, it has been observed that increasing the power density of the incident electron beam and/or decreasing the steady-state concentration of the precursor during deposition results in an increase in deposited metal content although no study to date has produced 100% metallic purity using such a strategy.[10,22,33–38] Substrate annealing during deposition decreases the residence time for both the adsorbed precursors and the volatile products of dissociation, and also effectively increases the purity of deposits formed by FEBIP.[39–41] Postdeposition annealing, either *in situ* or in the presence of a reactive species, can also result in increased deposition purity.[42–46] However, annealing strategies can result in physical deformation of the deposited structure, nullifying the advantages of using FEBIP to create well-defined structures with nanometer scale resolution. The introduction of reactive species, such as water, oxygen, or hydrogen gas, during deposition is also capable of increasing the metal content of FEBIP deposits.[26,47,48] For example, in the case of gold nanostructures deposited from $Au^{III}(hfac)Me_2$, this type of abatement strategy has resulted in a metallic content that increased from 3% to 50%.[49] However, complete purification has yet to be achieved and, furthermore, for some metals the use of oxidizing species promotes metal-oxide formation.[50–52] In principle, carbon-free precursors can circumvent the issues of organic contamination, although in practice their toxicity and instability make them poor candidates for larger scale application.[19,53]

The use of atomic radicals to remove organic contamination from FEBIP deposits is a promising, new purification strategy. For example, postdeposition exposure to atomic hydrogen has been used to increase the purity of platinum structures deposited from $MeCpPt^{IV}Me_3$ although the surface was concomitantly annealed to 130 °C.[54] In another relevant study of radical purification, transmission electron microscopy (TEM) images have shown that exposure of an electron beam deposited platinum field emitter device ($CpPt^{IV}Me_3$ precursor) to atomic oxygen resulted in a significant change to the material's grain structure suggesting that *in situ*, postdeposition exposure to atomic radicals at room temperature may improve the material's metal content.[55] In the present study, we have explored the abatement capabilities and surface reactions of atomic radicals, specifically atomic hydrogen (AH) and atomic oxygen (AO), using deposits formed from the electron beam induced decomposition of the gold precursor, $Au^{III}(acac)Me_2$. In an effort to mimic the deposition resolution of structures deposited using FEBIP, the thickness of these deposits has been limited to the nanometer regime.

AH and AO are highly reactive species that can chemically etch carbon atoms at ambient temperatures through the formation of volatile species.[56,57] In contrast to ions, AH and AO can etch carbon without any physical sputtering of adsorbed metal atoms. Atomic radicals can also be generated cleanly in a vacuum environment by passing the parent diatomic gas through a heated capillary.[58] Thus, AH and AO represent a potential *low temperature* route for the abatement of organic contamination from FEBIP deposited structures.

To understand the chemical and physical transformations that occur to FEBIP deposits exposed to atomic radicals, we have studied the interactions of AH and AO with electron beam deposited structures using an array of surface analytical techniques. To facilitate the use of traditional surface analytical techniques such as x-ray photoelectron spectroscopy (XPS) and scanning Auger electron spectroscopy (AES), we have shifted the paradigm from that of FEBIP deposited, three-dimensional, nanosized objects to nanometer scaled thin films with significantly larger ($0.1\ mm^2 - 1\ cm^2$) planar dimensions.[59,60] To complement the chemical information provided by XPS and AES, we have also used atomic force microscopy (AFM) to probe changes in the physical structure of the electron beam deposits that occur as a result of radical (AH and AO) exposure.

II. EXPERIMENTAL METHODS

A. Precursor

Dimethyl-(acetylacetonate) gold(III) [Strem Chemicals; $Au^{III}(acac)Me_2$], was used as the precursor for the deposition of gold-containing thin films. $Au^{III}(acac)Me_2$ is a volatile, crystalline solid that sublimes at ≈25 °C. Prior to introduction into any of the ultra high vacuum (UHV) chambers, the $Au^{III}(acac)Me_2$ was stored in a glass finger attached to a gas manifold via a glass-to-metal seal. During deposition, the precursor was dosed through an UHV compatible leak valve and the gas purity was routinely checked by mass spectrometry (Stanford Research Systems, 0–200 amu).

B. Radical treatment

The effect of atomic radicals on electron beam deposited gold-containing films was studied *in situ* in two UHV chambers, one equipped with capabilities for XPS and the other with capabilities for scanning AES; *ex situ* analysis of films deposited in the AES chamber was also performed using AFM. In both XPS and AES chambers, atomic radicals were generated in a thermal gas cracker (Oxford Applied Research) by passing either H_2 or O_2 through a heated Ir capillary (inside diameter of ≈2.0 mm) to produce a directed flux of atomic radicals (80%–90% dissociation efficiency based on manufacturer's estimate).[58,61] The radical source was positioned perpendicular to the substrate at a distance of ≈7.0 cm in the XPS chamber and an incident angle of ≈45° at a distance of ≈5.0 cm in the AES chamber. There was no measurable increase in substrate temperature during experi-

ments performed with the thermal gas cracker. To optimize the efficiency of radical production, the source operates at 60 and 30 W for AH and AO productions, respectively, in accordance with the manufacturer's recommendations. To maintain a constant flux of atomic radicals at the surface, the flow of either H_2 or O_2 through the source was held constant, as measured by the pressure within the UHV chamber. In the XPS system, the flux of atomic radicals was estimated to be $\approx 5\times10^{15}$ H atoms s^{-1} cm^{-2} ($P_{H_2}=1.5\times10^{-5}$ Torr) and $\approx 2\times10^{14}$ O atoms s^{-1} cm^{-2} ($P_{O_2}=6.0\times10^{-7}$ Torr). In the AES system, the radical flux was estimated to be $\approx 3\times10^{15}$ H atoms s^{-1} cm^{-2} ($P_{H_2}=5.0\times10^{-6}$ Torr) and $\approx 3\times10^{14}$ O atoms s^{-1} cm^{-2} ($P_{O_2}=5.0\times10^{-7}$ Torr). Atomic radical flux values were estimated from previous studies, assuming that the thermal cracker acts as an effusive source.[61]

C. AES studies

Ag foil was used as the substrate in AES experiments. In these studies, the substrate was affixed to a stainless steel stub and introduced into the vacuum chamber via a load lock chamber where the sample rested on a stage with *XYZ* translational and 60° rotational capabilities. Ag substrates were routinely cleaned with 2.5 keV Ar^+ and substrate cleanliness was verified with AES.

In the AES chamber (Phi 610), electron beam deposited films were created at room temperature by rastering the instrument's electron beam (≈ 1.5 μm spot size, 1.5 keV incident energy) for 20–60 min over a well-defined region of the Ag substrate, in the presence of a constant partial pressure ($\approx 1.0\times10^{-7}$ Torr) of $Au^{III}(acac)Me_2$. The incident electron beam had a power density of $\approx 2\times10^{2}$ $\mu W/\mu m^2$ and the substrate was at room temperature. Film thicknesses were not quantified in AES experiments.

In AES experiments, the two-dimensional size and structure of films deposited by electron irradiation were determined using the system's secondary electron detector (SED), while the film's chemical composition was determined by AES using 3 keV electrons. In Auger maps, the spatial distribution of surface gold and carbon concentrations were obtained by measuring the difference in AES signals observed at an energy corresponding to either a gold ($Au_{MNN}\approx 67$ eV) or carbon ($C_{KLL}\approx 262$ eV) Auger transition and a proximate electron energy that did not correspond to any Auger transition (background signal). Oxygen AES maps could not be obtained due to the lower surface concentration of oxygen in the films coupled with a greater difficulty in separating the oxygen AES transition from the background.

D. XPS studies

For XPS measurements, a polycrystalline Ag foil (Aldrich; 1.5 cm^2) was used as the substrate although a small number of control studies were also performed on SiO_2 (1.5 cm^2). Ag was selected as a substrate because (a) the $Au^{III}(acac)Me_2$ did not decompose on Ag at low temperatures and (b) Ag has an XP spectrum that does not interfere with any of the precursor elements (Au, C, and O). Ag or SiO_2 substrates were mounted at the end of a manipulator arm using a Ta holder with capabilities for *XYZ* translation and 360° rotation. A type *K* thermocouple was adhered to the underside of the sample holder to measure temperature. Substrates were routinely cleaned by sputtering with 2–4 keV Ar^+. On sputter cleaned silicon substrates, the oxide layer was replenished by exposure to atomic oxygen. Surface cleanliness prior to film deposition was routinely checked by XPS.

The creation of planar (>1 cm^2) electron beam deposits from $Au^{III}(acac)Me_2$ proceeded via several steps; first, nanometer scale thick adlayers of $Au^{III}(acac)Me_2$ were generated by directionally dosing the precursor through an UHV compatible leak valve onto the substrate through a metal tube, producing a chamber pressure of $\approx 1\times10^{-7}$ Torr. During $Au^{III}(acac)Me_2$ deposition, substrate temperatures were maintained at $\approx$160 K to allow precursor adsorption to occur without concomitant adsorption of low molecular weight contaminants. Once deposited, this molecular $Au^{III}(acac)Me_2$ adlayer was exposed to 30 min of broad beam electron irradiation using a commercial flood gun (Specs 15/40) positioned perpendicular to the substrate at a distance of $\approx$12 cm. The incident electron energy was 520 eV and the resultant power density was $\approx 1.7\times10^{-4}$ $\mu W/\mu m^2$. Previous studies have established that this method results in the complete electron stimulated decomposition of all precursor molecules and the formation of an electron beam deposited film that contains gold atoms embedded in an organic matrix containing carbon and oxygen.[62] Once formed, the substrate was allowed to return to room temperature prior to either AH or AO exposure.

XPS analysis of all films was performed *in situ* using a Physical Electronics 5400 system and x-rays generated from a magnesium anode (Mg $K\alpha$ 1253.6 eV) operating at 300 W. Ejected photoelectrons were analyzed by a multichannel hemispherical analyzer. XP peak positions for experiments conducted on Ag substrates were referenced to the $Ag(3d_{5/2})$ peak at 368.3 eV; for consistency the SiO_2 XP peaks were calibrated to the $Au(4f_{7/2})$ peak positions, Au^{III} at 86.0 eV and Au^0 at 84.0 eV, established during experiments performed on the Ag substrate. Film compositions were measured at a pass energy of 90 eV, while more detailed spectral analysis of the O(1*s*), C(1*s*), and Au(4*f*) regions were obtained using a pass energy of 22 eV; relative sensitivity factors used were 6.25 [Au(4*f*)], 0.296 [C(1*s*)], and 0.711 [O(1*s*)].[63]

For experiments performed on Ag substrates, average film thicknesses were calculated by measuring the attenuation of the Ag(3*d*) XP signal using Eq. (1),

$$\text{film thickness (nm)} = \left[-\lambda_{Ag(3d)}\cos(\theta)\ln\left(\frac{Ag}{Ag_0}\right)\right], \quad (1)$$

where λ is the inelastic mean free path of a Ag(3*d*) photoelectron (1.32 nm), θ is the photoelectron take-off angle (54°), and Ag_0 and Ag are the integrated areas of the Ag(3*d*) peaks before film deposition (i.e., clean Ag substrate) and

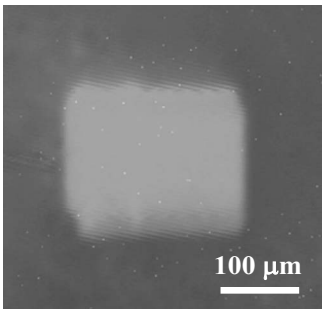

FIG. 1. Secondary electron image of an electron beam deposited film (230×190 μm^2) grown on a silver substrate by electron irradiation ($\approx1.9\times10^2$ $\mu W/\mu m^2$) in the presence of a constant partial pressure ($\approx1\times10^{-7}$ Torr) of $Au^{III}(acac)Me_2$ for 20 min.

after electron beam irradiation of the $Au^{III}(acac)Me_2$ adlayer, respectively.[64]

E. AFM studies

Atomically flat and conductive, highly ordered pyrolytic graphite (HOPG) (SPI Supplies; 1.6 cm^2) was used as the substrate for AFM studies. *Ex situ* morphological analysis of electron beam deposited films grown onto HOPG substrates within the AES chamber was performed before and after the films had been exposed to atomic radicals. This was accomplished by removing HOPG substrates from the vacuum chamber and adhering them to the AFM sample plate using double-sided carbon tape. SED images, obtained within the AES chamber, were used in conjunction with physical markers scribed into the HOPG surface to help locate the position of the deposit using the optical microscope attached to the AFM. To provide better contrast between the deposited material and the HOPG substrate, the AFM tip was used in certain instances to remove deposits from a selected area within the deposition region. This was accomplished by decreasing the tip's oscillatory amplitude, thereby increasing the force exerted by the tip on the surface and removing the deposits.[65] AFM images were acquired using a PicoSPM LE (Agilent Technologies) operating in magnetic tapping mode using magnetically coated probes (Micromasch; NSC 18 Co/Cr) operating at an oscillating frequency of ≈80 kHz. All image rendering and height measurements were performed utilizing commercially available software from Agilent Technologies.

III. RESULTS

In the following, we report on the three experiments used to assess the impact of atomic radical (AH and AO) exposure on the composition of electron beam deposited films.

(i) A micron-scale film was grown in the AES system by rastering an electron beam over a well-defined region of the substrate (at room temperature) in the presence of a constant partial pressure of precursor molecules. A SED image of a structure deposited in this way is shown in Fig. 1. AES was used *in situ* to examine the changes in chemical composition that occurs when these electron beam deposited films are exposed to atomic radicals (AH or AO).

(ii) A film was deposited over a large surface area (>1 cm^2) by the electron irradiation of an adsorbed layer of $Au^{III}(acac)Me_2$; the effect of AH and AO on these electron beam deposited films was then analyzed *in situ* and at room temperature by XPS.

(iii) *Ex situ* AFM analysis was performed on a film, electron beam deposited in the AES chamber, before and after sequential exposure to AO and AH. These experimental approaches are summarized in Table I.

A. Impact of AH exposure on electron deposited films

Figure 2 shows carbon and gold Auger maps for an electron beam deposited structure before (left) and after (center) prolonged exposure to AH (64.5 h). After AH treatment, the carbon AES signal has diminished significantly producing a structure predominantly composed of gold. Representative line scans through carbon and gold Auger maps before and after AH exposure are shown in Fig. 2 (right), highlighting the almost complete loss of carbon from the structure as a result of AH exposure.

Figures 3(a) and 3(b) illustrate the changes in the Au($4f$), C($1s$), and O($1s$) regions that occur when $Au^{III}(acac)Me_2$ films are exposed to electron irradiation. In Fig. 3(a), the XP spectra of a ≈2.8 nm thick $Au^{III}(acac)Me_2$ film molecularly adsorbed onto Ag at ≈160 K is shown. The Au($4f_{7/2}$) peak of the adsorbed precursor is located at ≈86.2 eV, typical of gold atoms in a highly oxidized (+3) state.[66] In Fig. 3(a), the C($1s$) region exhibits two distinct features; one at ≈284.5 eV is representative of sp^3 hybridized carbon atoms (C–C, CH_2). The smaller spectral feature at ≈286.7 eV in the C($1s$) region, along with the corresponding peak at ≈532 eV in the O($1s$) region, is indicative of the C–O species in the acety-

TABLE I. Various surface analytical techniques employed in this study and the information obtained on electron beam deposited films.

Information provided by analytical method	AES (*in situ*) spatially resolved change in composition	XPS (*in situ*) change in composition and chemical bonding	AFM (*ex situ*) change in the size of deposits
Substrate(s)	Ag	Ag, SiO_2	HOPG
AH treatment	√	√	
AO treatment	√	√	
Sequential AO and then AH treatment	√	√	√

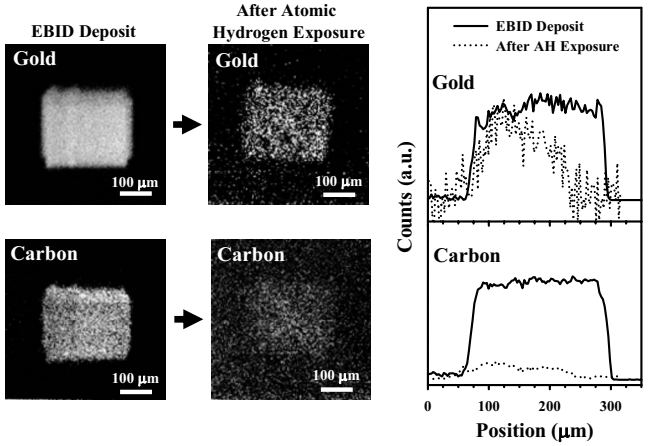

FIG. 2. (Left) Gold and carbon Auger maps of a film grown by electron beam induced deposition (EBID) on a silver substrate by rastering the electron beam ($\approx 2.2\times10^{2}$ μW/μm^2) over a defined region of the silver substrate for 1 h in the presence of a constant partial pressure ($\approx 1\times10^{-7}$ Torr) of $Au^{III}(acac)Me_2$. (Center) Auger maps of the same film after exposure to atomic hydrogen for 64.5 h ($P_{H_2}=6\times10^{-6}$ Torr; $\approx 3.8\times10^{15}$ H atoms s^{-1} cm^{-2}). (Right) Gold and carbon Auger line scans illustrate the changes in film composition as a result of atomic hydrogen treatment.

lacetonate ligand. Electron irradiation (1.7×10^{-4} μW/μm^2, 30 min) of the $Au^{III}(acac)Me_2$ film leads to the XP spectra shown in Fig. 3(b). Compared to Fig. 3(a), the Au($4f_{7/2}$) peak has shifted to lower binding energy, ≈83.8 eV. This is consistent with the reduction in Au atoms from a Au^{III} oxidation state to a zero valent, Au^0, metallic state.[63] In the C(1*s*) region, the C–C/CH_2 feature at 284.5 eV broadens and increases slightly in intensity, while in contrast the C–O features at 286.7 and 532 eV decreased in intensity after electron irradiation. Previous studies have shown that

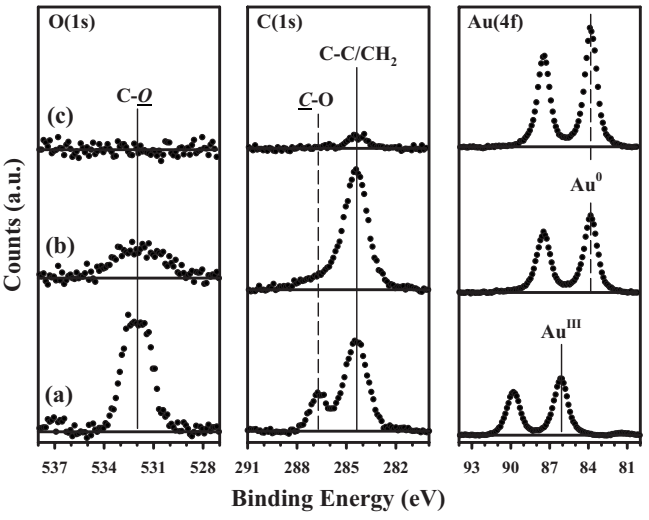

FIG. 3. XP spectra of the Au(4*f*), C(1*s*), and O(1*s*) regions of (a) a 2.8 nm thick molecularly adsorbed $Au^{III}(acac)Me_2$ film on a silver substrate at ≈160 K, (b) the same film after electron irradiation ($\approx 1.7\times10^{-4}$ μW/μm^2, 30 min), and (c) the electron beam deposited film after 35 h exposure to atomic hydrogen ($P_{H_2}=\approx 1\times10^{-5}$ Torr; $\approx 3.3\times10^{15}$ H atoms s^{-1} cm^{-2}).

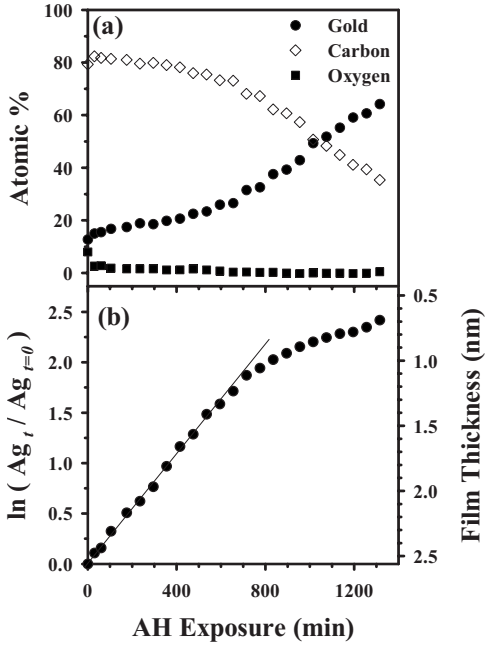

FIG. 4. (a) Changes in the elemental composition of a 2.6 nm thick electron beam deposited film, as a function of atomic hydrogen exposure ($P_{H_2}=1.5\times10^{-5}$ Torr, $\approx 4.9\times10^{15}$ H atoms s^{-1} cm^{-2}). (b) The corresponding change in the film thickness during atomic hydrogen exposure has been determined by Eq. (1); a best-fit line has been fit through the region where the film thickness decreases linearly with atomic hydrogen exposure.

changes in the O(1*s*) and C(1*s*) regions are due predominantly to CO and CH_4 production.[62] After electron beam irradiation, the elemental composition of the electron deposited film shown in Fig. 3(b) is 12% gold, 80% carbon, and 8% oxygen.

The spectra in Fig. 3(c) shows the XP spectra obtained after the electron beam deposited film, shown in Fig. 3(b), was exposed to AH for 35 h; further AH exposure produced no further changes in the film's composition. A comparison of Figs. 3(b) and 3(c) reveals that exposure to AH removed all of the intensity within the O(1*s*) region while the C(1*s*) signal also significantly decreased in intensity, although a small peak centered at 284.5 eV is still visible. The analysis of Fig. 3(c) reveals that AH exposure also increased the Au(4*f*) signal intensity. At the conclusion of the AH treatment, the film's composition was 75% gold, 24% carbon, and <1% oxygen. It should be noted that these changes in chemical composition, observed by XPS, are also qualitatively consistent with the effects of AH exposure shown by the AES results shown in Fig. 2.

Figure 4(a) shows how the chemical composition of an electron deposited film produced from the decomposition of $Au^{III}(acac)Me_2$ changes as a function of AH exposure time. The initial composition of the deposited film was 12% gold, 80% carbon, and 8% oxygen. For comparatively short AH exposures (<30 min), changes in film composition were dominated by the loss of oxygen. For more prolonged AH exposures, a systematic loss of carbon and residual oxygen from the film is accompanied by a steady increase in the gold XPS signal. Figure 4(b) shows how the average film thick-

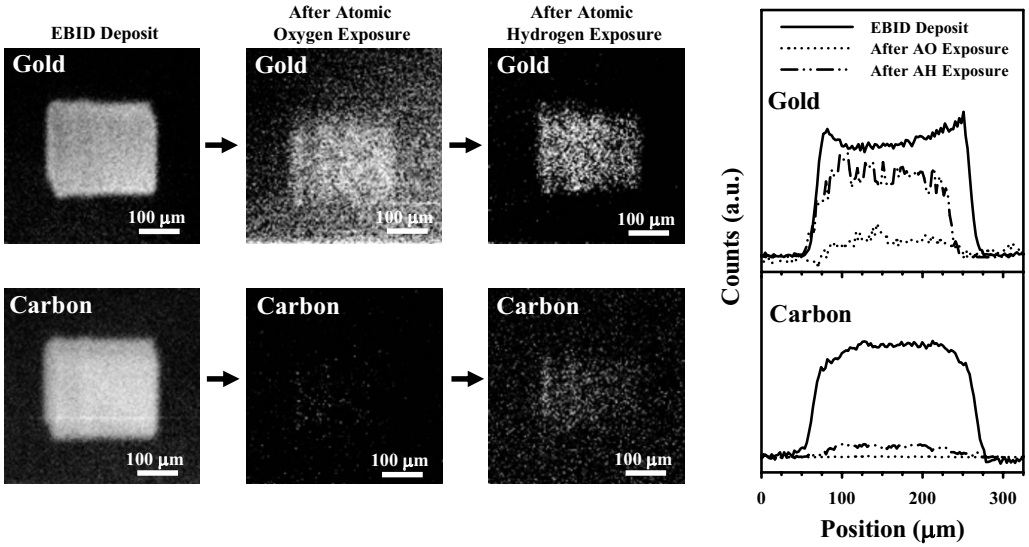

FIG. 5. (Left) Gold and carbon Auger maps of a film grown by EBID on a silver substrate by rastering an electron beam ($\approx 1.9\times10^{2}$ μW/μm^2) over a defined region of the silver substrate for ≈20 min in the presence of a constant partial pressure ($\approx 1\times10^{-7}$ Torr) of $Au^{III}(acac)Me_2$. (Left center) Auger maps of the film after exposure to atomic oxygen for ≈48 h ($P_{O_2}=5.5\times10^{-7}$ Torr; $\approx 3.5\times10^{14}$ O atoms s^{-1} cm^{-2}) and (right center) after the same film was subsequently exposed to atomic hydrogen ($P_{H_2}=5.0\times10^{-6}$ Torr; $\approx 3.2\times10^{15}$ H atoms s^{-1} cm^{-2}) for 0.4 h. (Right) Representative gold and carbon Auger line scans of the film after deposition and then after subsequent atomic oxygen and then atomic hydrogen exposures illustrate the changes in the film's composition at each step.

ness [calculated by Eq. (1)] changes as a function of AH exposure. For AH exposures <700 min, the average film thickness decreases linearly with AH exposure at a rate of 1.2 Å/h [see line in Fig. 4(b)] due to the etching of carbon and oxygen (principally carbon) from the film; after >700 min of AH exposure, the etch rate slowed. The film's composition after ≈22 h of AH exposure was 64% gold, 35% carbon, and <1% oxygen.

B. Effect of AO followed by AH exposure on electron deposited films

Figure 5 illustrates the changes in the gold and carbon AES maps for an electron beam deposited structure (left) that was sequentially exposed to AO for ≈48 h (left center) and then AH for ≈40 min (right center). After AO exposure, the AES signal in both the gold and carbon Auger maps had decreased. There was no visual evidence of residual carbon in the structure, although the location of the deposit could still be discerned from the gold AES map. Following subsequent AH exposure there was a noticeable increase in the sharpness of the gold AES map. Representative gold and carbon AES line scans at various stages of the film's modification are also shown on the right hand side of Fig. 5. These AES maps highlight the loss of carbon from the film that occurs after AO exposure and the increase in gold signal that occurs after the AO treated film was subsequently exposed to AH.

In Figs. 6(a) and 6(b), the spectral envelopes and peak positions in the Au(4*f*), C(1*s*), and O(1*s*) regions are consistent with the spectra shown in Figs. 3(a) and 3(b) for a $Au^{III}(acac)Me_2$ film before and after electron irradiation, respectively. The elemental composition of the electron beam deposited film in Fig. 6(b) was calculated to be 10% gold, 80% carbon, and 10% oxygen and the film's thickness was estimated to be ≈1.1 nm. In Figs. 6(c) and 6(d), the effects of sequentially exposing this electron beam deposited film to AO [Fig. 6(c)] and then AH [Fig. 6(d)] are shown. In Fig. 6(c), the electron beam deposited film has been exposed to AO for 30 h resulting in *complete* loss of the film's carbon content. In addition to the loss of carbon, AO exposure also produced new spectral features at ≈528.4 eV in the O(1*s*) region and ≈85.0 eV in the Au(4*f*) region, the latter ob-

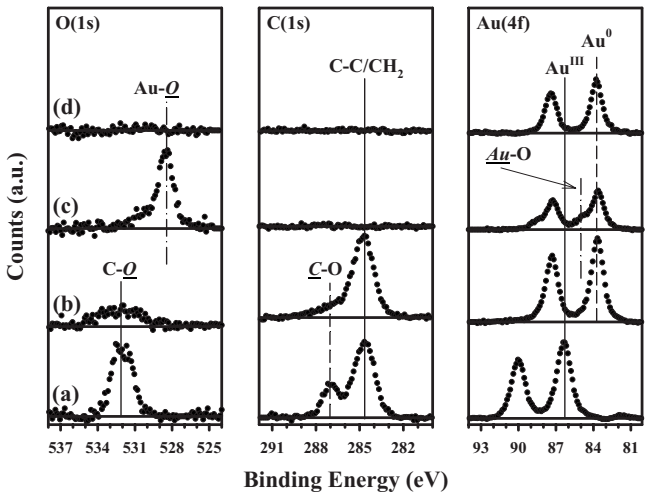

FIG. 6. XP spectra of the Au(4*f*), C(1*s*), and O(1*s*) regions for (a) a 2.5 nm thick molecularly adsorbed $Au^{III}(acac)Me_2$ film on a silver substrate at ≈160 K, (b) the same film after electron irradiation ($\approx 1.7\times10^{-4}$ μW/μm^2, 30 min), (c) the electron deposited film (≈295 K) after 30 h exposure to atomic oxygen ($P_{O_2}=6.0\times10^{-7}$ Torr; $\approx 2.0\times10^{14}$ O atoms s^{-1}cm^{-2}), and (d) after 1 h subsequent exposure to atomic hydrogen ($P_{H_2}=1.0\times10^{-5}$ Torr; $\approx 3.3\times10^{15}$ H atoms s^{-1} cm^{-2}).

TABLE II. Summary of XPS results obtained on the effect of atomic oxygen and/or atomic hydrogen on electron bean deposited films (* represents average values obtained from several electron beam deposited films).

	Au (at. %)	C (at. %)	O (at. %)
Molecularly adsorbed $Au^{III}(acac)Me_2$ film	10	70	20
Electron beam deposited film*	≈11	≈80	≈9
Effect of AH treatment	75	24	<1
Effect of AO treatment	14	0	86
Effect of sequential AO and then AH treatment	100	0	0

served as a shoulder to the higher binding energy side of the primary Au^0 peak at 83.8 eV. The positions of these new spectral features in the Au(4*f*) and O(1*s*) regions are consistent with the formation of a gold oxide.[67] The overall integrated intensity in the Au(4*f*) region also decreased as a result of AO exposure. It should be noted that the loss of carbon and the decrease in gold signal upon AO exposure are both consistent with the AES data shown in Fig. 5. After 30 h of exposure to AO, the resultant film's elemental composition was calculated to be 14% gold, 0% carbon, and 86% oxygen. Upon exposing this film to AH for 1 h, all of the oxygen was removed, the higher binding energy feature in the Au(4*f*) region disappeared and the residual film is 100% gold. Changes in the composition of the film, measured by XPS, as a result of electron stimulated decomposition and subsequent treatment by atomic radicals, are summarized in Table II.

Figure 7 explicitly considers, as a function of AO exposure, the variation in the chemical composition [Fig. 7(a)] and film thickness [Fig. 7(b)] of an electron deposited film produced from the decomposition of an adsorbed $Au^{III}(acac)Me_2$ adlayer. Thus, Fig. 7 is an analog of Fig. 4. In Fig. 7, the elemental composition of the film prior to AO exposure was 10% gold, 80% carbon, and 10% oxygen. In contrast to the effects of AH, comparatively short AO exposure (<100 min) produced an immediate increase in oxygen content within the film, as shown in Fig. 7(a). During this initial time interval, the gold XPS signal decreased slightly, while the average film thickness actually increases [see Fig. 7(b)]. For more prolonged AO exposures (>100 min), the oxygen and gold contents in the film gradually increase while the carbon content and film thickness exhibit a systematic decrease. Analogous to the effect of AH, the decrease in film thickness exhibits a linear dependence on AO exposure [see line in Fig. 7(b); 0.28 Å/h] over a wide range of intermediate AO exposures (≈100→900 min). After ≈17 h of AO exposure, the composition of the film is 17% gold, 31% carbon, and 52% oxygen. As shown in Fig. 6, even more prolonged AO exposures continue to reduce the surface carbon concentration until it falls below the XPS detection limit.

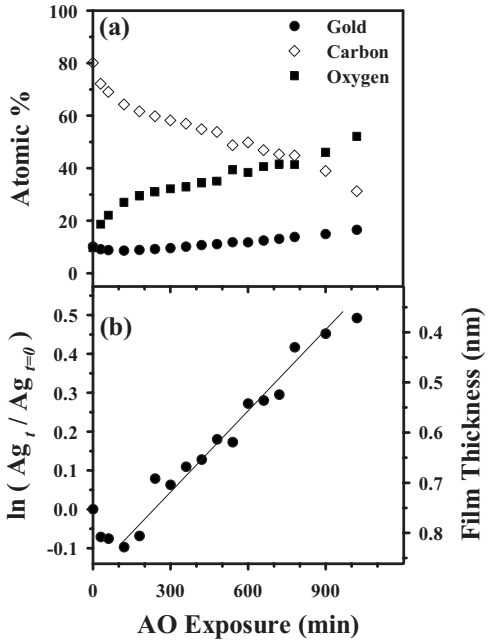

FIG. 7. (a) Changes in the elemental composition of a 0.76 nm thick gold, carbon, and oxygen film, formed by electron beam irradiation (≈1.7 $\times 10^{-4}$ $\mu W/\mu m^2$, 30 min) of $Au^{III}(acac)Me_2$, as a function of atomic oxygen exposure ($P_{O_2}=6.0\times10^{-7}$ Torr; $\approx 2.0\times10^{14}$ O atoms s^{-1} cm^{-2}). (b) The corresponding change in the film thickness during atomic oxygen exposure has been determined by Eq. (1); a best-fit line has been fit through the region where the film thickness decreases linearly with atomic oxygen exposure.

C. AFM studies

The morphological effects of sequential AO and AH exposures on electron beam deposited films are shown by the AFM images in Fig. 8. In these experiments, films were deposited by rastering a focused electron beam over the ≈400×500 μm^2 region of a HOPG substrate in the presence of a constant partial pressure of $Au^{III}(acac)Me_2$. In Fig. 8(a), a topographic AFM image of the as deposited structure is shown adjacent to the HOPG substrate; the presence of gold exclusively within the deposition region was also verified using AES. The discrete, spherical shaped objects in Fig. 8(a) have therefore originated from the electron induced decomposition of $Au^{III}(acac)Me_2$ molecules. An AFM image of the same structures after AO exposure for 40 h and subsequent AH exposure for 1 h is shown in Fig. 8(b). Both the planar scale and the height scale in Figs. 8(a) and 8(b) have been held constant; as a result, a visual comparison of Figs. 8(a) and 8(b) highlights the decrease in size that occurs as a result of AO and AH exposures. This is shown more explicitly in the normalized histograms of height distributions for the deposited structures, Fig. 8(c). For the as deposited electron beam structures (top) there is a broad height distribution that ranges from 9 to 21 nm, while after subsequent AO and AH treatments (bottom) the height distribution is centered within the range of 7–15 nm. Analysis of the size distribution, using >450 measurements of individual structures,

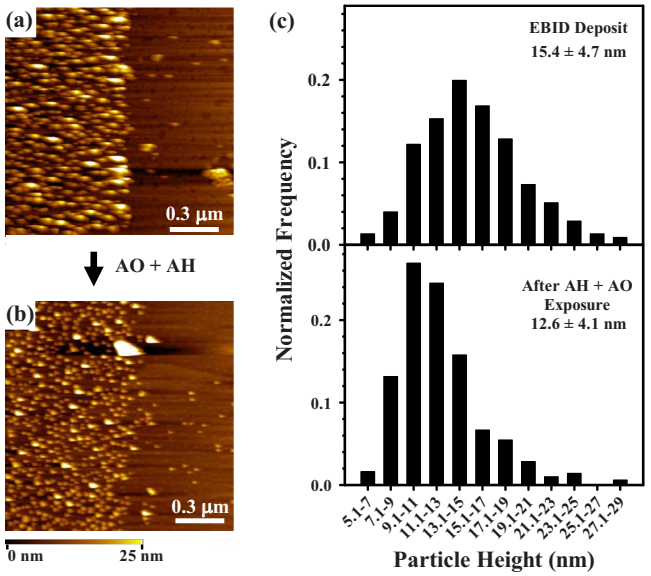

FIG. 8. (Color online) (a) Topographic AFM image of the structures formed by rastering an electron beam over a defined region of a HOPG substrate for 30 min in the presence of $\approx 1\times10^{-7}$ Torr $Au^{III}(acac)Me_2$. The HOPG was freshly cleaved between experiments. (b) Topographic AFM image of the electron beam deposited film after sequential exposure to atomic oxygen for 40 h ($P_{O_2}=5.5\times10^{-7}$ Torr; $\approx 3.5\times10^{14}$ O atoms s^{-1} cm^{-2}) and then 1 h atomic hydrogen ($P_{H_2}=5.0\times10^{-6}$ Torr; $\approx 3.2\times10^{15}$ H atoms s^{-1} cm^{-2}). (c) Particle height distribution measured by AFM for the electron beam deposited films before and after radical treatment.

reveals that the height distributions of the as deposited structures are 15.4 ± 4.7 and 12.6 ± 4.1 nm after radical treatment.

IV. DISCUSSION

Electron irradiation of the organometallic precursor, $Au^{III}(acac)Me_2$, produces a film with gold atoms embedded in an organic matrix containing oxygen and carbon atoms. The analysis of the XP data indicates that the average composition of the electron beam deposited film can be represented as $AuC_6O_{0.8(s)}$, while previous studies have shown that electron irradiation completely dehydrogenates the resultant film.[62] In the following discussion, we consider the surface reactions and mechanisms that characterize the interactions of AH and AO with an electron beam deposited film, including the effect of radical treatment on the deposits' structure.

A. Effect of AH on electron beam deposited films

AH reacts with surface oxygen and carbon to form volatile products while surface deposited gold atoms are unaffected. Previous studies have shown that AH reacts with carbon and oxygen-containing materials via a kinetically favorable Eley–Rideal-type mechanism.[68–72] Surface oxygen is removed by AH to form surface hydroxyl functional groups that are then further hydrogenated to form water, which desorbs.[68,71] Indeed, density functional calculations have determined that the hydrogenation of surface hydroxyl groups to form water is so favorable that it occurs without an activation barrier.[68] The AH abstraction of oxygen is summarized in Eqs. (2) and (3),

$$AH_{(g)} + \succ O_{(s)} \rightarrow\ \rightarrow \succ OH_{(s)}, \tag{2}$$

$$AH_{(g)} + \succ OH_{(s)} \rightarrow\ \rightarrow \succ H_2O_{(g)}\uparrow. \tag{3}$$

In contrast, surface carbon reacts with AH to form successively increasingly hydrogenated carbon species (e.g., CH_2 then CH_3), with carbon atoms ultimately leaving the surface in the form of a low molecular weight hydrocarbon species (i.e., methane, ethane, and ethene), as shown in Eq. (4),[73]

$$AH_{(g)} + \succ C_{(s)} \rightarrow\ \rightarrow \succ CH_{(s)} \xrightarrow{\text{many steps}} C_xH_{y(g)}\uparrow. \tag{4}$$

There is, however, a competing reaction for the consumption of incident AH; surface hydrogen abstraction to form hydrogen gas. Hydrogen abstraction by incident AH, shown in Eq. (5), is a common phenomenon and has been observed in the cross linking of long chained alkanethiolate self-assembled monolayers as well as in the temperature dependent etching of graphite by AH,[70,73,74]

$$AH_{(g)} + \succ CH_{(s)} \rightarrow\ \rightarrow \succ C_{(s)} + H_{2(g)}\uparrow. \tag{5}$$

At ambient temperatures the removal of carbon [Eq. (4)] by AH occurs at a slower rate than hydrogen abstraction, Eq. (5).[73] As a result, AH induced etching of carbon contamination is not a particularly efficient process.

The analysis of Fig. 4 reveals that AH etching of carbon atoms produces a linear decrease in the film's thickness over a wide range of AH exposures (0–700 min). Such a behavior is indicative of zeroth-order kinetics resulting from a steady-state etching process due to the fact that the penetration depth of AH is less than the film's thickness.[67] For sufficiently prolonged AH exposures, as the thickness of the contaminant layer decreases, a point is reached at which the penetration depth of incident AH atoms becomes comparable to the thickness of the remaining film. Under these conditions, the etch rate decreases as the remaining carbon atoms can react with *all* of the incident AH, leading to first-order kinetics. The fact that there is residual carbon remaining in the deposit even after the longest AH exposures suggests that there is a small amount of "hard" or diamondlike carbon present which AH cannot etch.[75]

In summary, the reactions of AH with the electron beam deposited film can be summarized by Eq. (6),

$$\begin{aligned} AH_{(g)} + Au^0C_6O_{0.8(s)} \rightarrow\ \rightarrow\ & Au^0C_{z(s)} \\ & + C_xH_{y(g)}\uparrow(\text{principally } CH_4) \\ & + H_2O_{(g)}\uparrow. \end{aligned} \tag{6}$$

B. Effect of AO on electron beam deposited films

Carbon and oxygen atoms are both efficiently etched from the electron beam deposited film as a consequence of AO exposure due to the formation of volatile species, specifically

CO and CO_2.[56] Based upon previous studies of AO reactions with amorphous carbon (a:C) films, the overall mechanism can be described by an initial step which consists of oxygen addition to the film to form surface bound oxygen-containing functional groups (CO_x species) followed by the subsequent reactions of these CO_x groups to form volatile CO and CO_2 species.[67,76] This can be described symbolically as shown below,

$$AO_{(g)} + a{:}C_{(s)} \rightarrow \rightarrow > CO_{x(s)}, \quad (7)$$

$$AO_{(g)} + > CO_{x(s)} \rightarrow \rightarrow CO_{(g)}/CO_{2(g)}. \quad (8)$$

Figure 6(c), as well as the AES maps and line scans in Fig. 5, show that prolonged AO exposure removes all carbon from the film, consistent with the greater etching efficiency of AO compared to AH.[77] In addition to carbon removal, AO can also react with gold to form Au–O bonds; this is evidenced experimentally by the new O(1s) and Au(4f) features that appear at ≈528.4 and ≈85.0 eV after prolonged exposure of the electron beam deposited film to AO.[67] Thus, although AO effectively removes organic carbon and oxygen from the film, the resultant film is not pure metallic gold due to the presence of Au–O species. Indeed, the oxidation of gold atoms by AO is likely responsible for the decrease in the Au XPS and AES signals in Figs. 5 and 6(c).

In contrast to the effect of AH, the film thickness increases during the initial stages of AO exposure. This can be rationalized in terms of the AO etching mechanism outlined in Eqs. (7) and (8). For short AO exposures, the etching process is dominated by the addition of oxygen into the film [Eq. (7)]. This assertion is also supported in XPS studies by an increase in the O(1s) peak at ≈287 eV associated with C–O species in the film during the initial stages of the reaction—data not shown. As a consequence of this oxygen addition, there is an increase in the attenuation of the Ag(4f) substrate photoelectrons producing an increase in the measured film thickness. This regime is absent for AH etching due to the negligible effect that hydrogen addition has on the attenuation of substrate photoelectrons.

Once a sufficient amount of oxygen has been added to the film, however, a steady-state etch front forms due to the limited penetration depth of AO within carbonaceous films.[67] As a result of this steady-state etch front, an extended time regime exists over which a linear decrease in the film's thickness is observed with increasing AO exposure [Fig. 7(b)], consistent with a zeroth-order kinetic process and analogous to the situation observed for AH [Fig. 4(b)]. For the more prolonged AO exposures necessary to remove all of the adsorbed carbon (>22 h shown in Fig. 7), the etching kinetics should transition to a first-order process when the remaining film thickness reaches the point where it is on the same scale as the AO penetration depth, analogous to what was observed with AH (Fig. 4). Indeed, such a transformation has been observed previously in the reactions of AO with nanometer scale thin carbonaceous films.[67]

C. Comparison of AH and AO etching

Using the steady-state etch rates of AH and AO, 1.2 and 0.28 Å/h, respectively, determined from Figs. 4(b) and 7(b), a semiquantitative comparison of the etching efficiencies of these two atomic radicals can be made. Based on previous studies, where we have determined that the flux of AH produced by the thermal cracker varies linearly as a function of the gas pressure in the chamber, and assuming that the thermal cracker acts as an effusive source and furthermore that the efficiency of AH and AO production from H_2 and O_2 is comparable, we estimate that the etching efficiencies are 2.6×10^{-20} nm/O atom and 4.7×10^{-21} nm/H atom.[61] Although qualitative, these values are consistent with the expectation that AO is more efficient at etching carbon and oxygen compared to AH. However, in an absolute sense neither AH or AO is particularly an efficient etching reagent.

D. Effect of sequential AO and AH exposure

Previous studies have shown that AH can effectively reduce surface oxides to form metallic overlayers.[78] Based on this observation, we exposed electron beam deposited films first to AO to remove all of the carbon atoms and then to AH to reduce the gold oxide species. Results from this combinatorial approach revealed that a deposit consisting of pure gold atoms could be formed, free from any carbon or oxygen contamination. Furthermore, the time required to reduce all Au–O species using AH was relatively short, indicating an efficient process compared to the carbon etching. The only drawback with this approach was that in some cases AH exposure resulted in a reappearance of trace amounts of carbon in the deposit (see, for example, the carbon AES line scans in Fig. 5).

Despite the success of using AO followed by AH to produce pure gold deposits there was a reduction in the integrated gold signal for films exposed to AO and then AH when Ag was used as the substrate [see, for example, a comparison of the Au(4f) XP regions between Figs. 6(b) and 6(d)]. To address this issue, we performed analogous experiments on SiO_2 substrates [see supporting information, Fig. S1 (Ref. 79)]. In this case, there was a clear, measurable increase in the gold XP signal after AO and AH exposures, consistent with the anticipated effect of carbon and oxygen removal from the film. We believe that the decrease in Au(4f) signal intensity observed for deposits grown on Ag substrates is due to mixing of metallic Au and Ag atoms at the interface between these miscible elements during radical exposure, facilitated by the energy released as a result of the etching process.

E. Structural effects of radical treatment

In Fig. 8, the effects of AO and AH exposures on the structure of the electron beam deposited films are shown. The discrete, isolated deposits shown in Fig. 8(a) are representative of those formed by rastering the AES electron beam across a HOPG surface in the presence of the $Au^{III}(acac)Me_2$ precursor. Thus, collectively these structures comprise the

electron beam deposited films shown in the SED image of Fig. 1 and the carbon and gold AES maps in Figs. 2 and 5. Following AO and then AH exposure, the size of the deposits has decreased appreciably as a consequence of the carbon and oxygen being removed [compare Figs. 8(a) and 8(b)]. The etching of carbon and oxygen, however, does not change the isolated and discrete nature of the structures present.

Based on the average chemical composition of the electron beam deposits ($AuC_6O_{0.8}$) and the atomic radii of the constituent elements, the loss of all carbon and oxygen from the film would produce an ≈50% decrease in the volume of material present within the deposits. If we assume that the deposited structures are approximately spherical in shape, then we would predict that the removal of all organic material from the FEBIP deposits would decrease the average height of the deposits by 21%. This is comparable to the 18% decrease in height that we observed experimentally, decreasing from 15.4 ± 4.7 to 12.6 ± 4.1 nm after radical treatment. The fact that the theoretical estimates and experimental observations are in good agreement with one another suggests that the electron beam deposited gold is not freely dispersed within the deposited organic matrix but does in fact self-segregate into a close packed arrangement. This is consistent with previous studies, where cross sectional TEM images have shown the effect of AO exposure on FEBIP fabricated structures.[45,55]

The present study has focused on electron beam deposited films containing gold atoms. However, we anticipate that our results will apply to other metal-containing structures formed using FEBIP. Since other metals will also be susceptible to oxidation by AO, a combination of AO and AH will be needed to produce pure metallic structures from other electron beam deposits. Our studies have shown that AO and AH can effectively remove organic contamination from the nanometer thick films typically deposited in FEBIP. However, it would be useful to know if there is an upper limit to the film thickness that can be purified using the atomic radicals described in this study. Other issues that merit further investigation include developing approaches to accelerate the etching rate (for example, by exploiting synergistic effects between different reactive species, such as electrons and radicals that are often crucial in plasma processes) and exploring the potential of radicals to affect *in situ* purification during the FEBIP process as opposed to a postdeposition purification strategy.

V. CONCLUSIONS

Both atomic hydrogen (AH) and atomic oxygen (AO) are capable of removing oxygen and carbon atoms from the organic matrix that forms during the electron stimulated decomposition of $Au^{III}(acac)Me_2$, although the extent of carbon removal and the etching efficiency are greater for AO. Pure gold deposits can be formed at room temperature by sequentially exposing nanometer scale FEBIP deposits to AO and then AH. In this combinatorial radical treatment process, the initial AO treatment removes all of the nascent carbon atoms from the organic matrix, while the subsequent AH exposure reduces the gold oxide that forms as a side product during AO exposure. FEBIP deposits decrease in size when carbon and oxygen are removed, consistent with the formation of a dense, close packed array of gold atoms. In broader terms, the abatement strategies developed in this study should also be able to form pure metallic structures from FEBIP deposits that contain metals other than gold.

ACKNOWLEDGMENTS

The authors thank Willem F. van Dorp for his helpful comments. This research was funded by support from the National Science Foundation (Grant No. CHE-0616873). They also acknowledge the use of the surface analysis laboratory at Johns Hopkins University.

[1] I. Utke, P. Hoffman, and J. Melngailis, J. Vac. Sci. Technol. B **26**, 1197 (2008).
[2] W. F. van Dorp and C. W. Hagen, J. Appl. Phys. **104**, 081301 (2008).
[3] S. J. Randolph, J. D. Fowlkes, and P. D. Rack, Crit. Rev. Solid State Mater. Sci. **31**, 55 (2006).
[4] M. Tanaka, M. Shimojo, M. Han, K. Mitsuishi, and K. Furuya, Surf. Interface Anal. **37**, 261 (2005).
[5] W. F. van Dorp, C. W. Hagen, P. A. Crozier, and P. Kruit, Nanotechnology **19**, 225305 (2008).
[6] K. Edinger *et al.*, J. Vac. Sci. Technol. B **22**, 2902 (2004).
[7] T. Liang, E. Frendberg, B. Lieberman, and A. Stivers, J. Vac. Sci. Technol. B **23**, 3101 (2005).
[8] K. L. Lee, D. W. Abraham, F. Secord, and L. Landstein, J. Vac. Sci. Technol. B **9**, 3562 (1991).
[9] D. J. Keller and C. Chih-Chung, Surf. Sci. **268**, 333 (1992).
[10] I. Utke, T. Bret, D. Laub, P. A. Buffat, L. Scandella, and P. Hoffman, Microelectron. Eng. **73–74**, 553 (2004).
[11] I.-C. Chen, L.-H. Chen, C. Orme, A. Quist, R. Lal, and S. Jin, Nanotechnology **17**, 4322 (2006).
[12] I. Utke, B. Dwir, K. Leifer, F. Cicoira, P. Doppelt, P. Hoffman, and E. Kapon, Microelectron. Eng. **53**, 261 (2000).
[13] C. T. H. Heerkens, M. J. Kamerbeek, W. F. van Dorp, C. W. Hagen, and J. Hoekstra, Microelectron. Eng. **86**, 961 (2009).
[14] K. I. Schiffmann, Nanotechnology **4**, 163 (1993).
[15] H. W. P. Koops, J. Kretz, M. Rudolph, and M. Weber, J. Vac. Sci. Technol. B **11**, 2386 (1993).
[16] M. Weber, M. Rudolph, J. Kretz, and H. W. P. Koops, J. Vac. Sci. Technol. B **13**, 461 (1995).
[17] C. Schoessler and H. W. P. Koops, J. Vac. Sci. Technol. B **16**, 862 (1998).
[18] N. Silvis-Cividjian, C. W. Hagen, P. Kruit, M. A. d. Stam, and H. B. Groen, Appl. Phys. Lett. **82**, 3514 (2003).
[19] T. Brintlinger *et al.*, J. Vac. Sci. Technol. B **23**, 3174 (2005).
[20] G. C. Gazzadi and S. Frabboni, J. Vac. Sci. Technol. B **23**, L1 (2005).
[21] S. Frabboni, G. C. Gazzadi, L. Felisari, and A. Spessot, Appl. Phys. Lett. **88**, 213116 (2006).
[22] H. W. P. Koops, A. Kaya, and M. Weber, J. Vac. Sci. Technol. B **13**, 2400 (1995).
[23] P. D. Rack, J. D. Fowlkes, and S. J. Randolph, Nanotechnology **18**, 465602 (2007).
[24] T. Lukasczyk, M. Schirmer, H.-P. Steinruck, and H. Marbach, Langmuir **25**, 11930 (2009).
[25] I. Utke, A. Luisier, P. Hoffman, D. Laub, and P. A. Buffat, Appl. Phys. Lett. **81**, 3245 (2002).
[26] A. Perentes, G. Sinicco, G. Boero, B. Dwir, and P. Hoffman, J. Vac. Sci. Technol. B **25**, 2228 (2007).
[27] K. L. Lee and M. Hatzakis, J. Vac. Sci. Technol. B **7**, 1941 (1989).
[28] J. Kretz, M. Rudolph, M. Weber, and H. W. P. Koops, Microelectron. Eng. **23**, 477 (1994).
[29] I. Utke, P. Hoffman, B. Dwir, K. Leifer, E. Kapon, and P. Doppelt, J. Vac. Sci. Technol. B **18**, 3168 (2000).
[30] S. Graells, R. Alcubilla, G. Badenes, and R. Quidant, Appl. Phys. Lett. **91**, 121112 (2007).
[31] R. M. Langford, T.-X. Wang, and D. Ozkaya, Microelectron. Eng. **84**,

784 (2007).
[32]A. Botman, J. J. L. Mulders, and C. W. Hagen, Nanotechnology **20**, 372001 (2009).
[33]Y. M. Lau, P. C. Chee, J. T. L. Thong, and V. Ng, J. Vac. Sci. Technol. A **20**, 1295 (2002).
[34]I. Utke, V. Friedli, J. Michler, T. Bret, X. Multone, and P. Hoffman, Appl. Phys. Lett. **88**, 031906 (2006).
[35]K. L. Klein, S. J. Randolph, J. D. Fowlkes, L. F. Allard, H. M. Meyer III, M. L. Simpson, and P. D. Rack, Nanotechnology **19**, 345705 (2008).
[36]H. Plank, C. Gspan, M. Dienstleder, G. Kothleitner, and F. Hofer, Nanotechnology **19**, 485302 (2008).
[37]J. Li, M. Toth, V. Tileli, K. A. Dunn, C. J. Lobo, and B. L. Thiel, Appl. Phys. Lett. **93**, 023130 (2008).
[38]A. Fernández-Pacheco, J. M. De Teresa, R. Cordoba, and M. R. Ibarra, J. Phys. D: Appl. Phys. **42**, 055005 (2009).
[39]H. W. P. Koops, C. Schoessler, A. Kaya, and M. Weber, J. Vac. Sci. Technol. B **14**, 4105 (1996).
[40]S. Wang, Y.-M. Sun, Q. Wang, and J. M. White, J. Vac. Sci. Technol. B **22**, 1803 (2004).
[41]S. J. Randolph, J. D. Fowlkes, and P. D. Rack, J. Appl. Phys. **97**, 124312 (2005).
[42]A. Botman, J. J. L. Mulders, R. Weemaes, and S. Mentink, Nanotechnology **17**, 3779 (2006).
[43]M. H. Ervin, D. Chang, B. Nichols, A. Wickenden, J. Barry, and J. Melngailis, J. Vac. Sci. Technol. B **25**, 2250 (2007).
[44]S. Frabboni, G. C. Gazzadi, and A. Spessot, Physica E (Amsterdam) **37**, 265 (2007).
[45]K. Murakami *et al.*, Jpn. J. Appl. Phys. **48**, 06FF12 (2009).
[46]H. Hiroshima, N. Suzuki, N. Ogawa, and M. Komuro, Jpn. J. Appl. Phys., Part 1 **38**, 7135 (1999).
[47]R. M. Langford, D. Ozkaya, J. Sheridan, and R. Chater, Microsc. Microanal. **10**, 1122 (2004).
[48]K. Mølhave, D. N. Madsen, A. M. Rasmussen, A. Carlsson, C. C. Appel, M. Brorson, C. J. H. Jacobsen, and P. Boggild, Nano Lett. **3**, 1499 (2003).
[49]A. Folch, J. Tejada, C. H. Peters, and M. S. Wrighton, Appl. Phys. Lett. **66**, 2080 (1995).
[50]M. Shimojo, M. Takeguchi, and K. Furuya, Nanotechnology **17**, 3637 (2006).
[51]M. Shimojo, M. Takeguchi, K. Mitsuishi, M. Tanaka, and K. Furuya, Jpn. J. Appl. Phys., Part 1 **46**, 6247 (2007).
[52]M. Takeguchi, M. Shimojo, and K. Furuya, Jpn. J. Appl. Phys., Part 1 **46**, 6183 (2007).
[53]J. Barry, M. H. Ervin, J. Molstad, A. Wickenden, T. Brintlinger, P. Hoffman, and J. Meingailis, J. Vac. Sci. Technol. B **24**, 3165 (2006).
[54]A. Botman, M. Hesselberth, and J. J. L. Mulders, Microelectron. Eng. **85**, 1139 (2008).
[55]K. Murakami, S. Nishihara, N. Matsubara, S. Ichikawa, F. Wakaya, and M. Takai, J. Vac. Sci. Technol. B **27**, 721 (2009).
[56]J. D. Blackwood and F. K. McTaggart, Aust. J. Chem. **12**, 114 (1959).
[57]P. Tomkiewicz, A. Winkler, M. Krzywiecki, T. Chasse, and J. Szuber, Appl. Surf. Sci. **254**, 8035 (2008).
[58]U. Bischler and E. Bertel, J. Vac. Sci. Technol. A **11**, 458 (1993).
[59]J. D. Wnuk, J. M. Gorham, S. G. Rosenberg, W. F. van Dorp, T. E. Madey, C. W. Hagen, and D. H. Fairbrother, J. Phys. Chem. C **113**, 2487 (2009).
[60]W. F. van Dorp, J. D. Wnuk, J. M. Gorham, D. H. Fairbrother, T. E. Madey, and C. W. Hagen, J. Appl. Phys. **106**, 074903 (2009).
[61]J. D. Wnuk, J. M. Gorham, B. A. Smith, M. Shin, and D. H. Fairbrother, J. Vac. Sci. Technol. A **25**, 621 (2007).
[62]J. D. Wnuk, J. M. Gorham, S. G. Rosenberg, W. F. van Dorp, T. E. Madey, C. W. Hagen, and D. H. Fairbrother, J. Appl. Phys. **107**, 054301 (2010).
[63]J. F. Moulder, W. F. Stickle, P. E. Sobol, and K. D. Bomben, *Handbook of X-Ray Photoelectron Spectroscopy* (Physical Electronics USA, Inc., Chanhassen, 1995).
[64]S. Tanuma, C. J. Powell, and D. R. Penn, Surf. Interface Anal. **17**, 911 (1991).
[65]J. M. Gorham, J. D. Wnuk, M. Shin, and D. H. Fairbrother, Environ. Sci. Technol. **41**, 1238 (2007).
[66]S. K. Bhargava, F. Mohr, and J. D. Gorman, J. Organomet. Chem. **607**, 93 (2000).
[67]J. Torres, C. C. Perry, S. J. Bransfield, and D. H. Fairbrother, J. Phys. Chem. B **106**, 6265 (2002).
[68]A. Jelea, F. Marinelli, Y. Ferro, A. Allouche, and C. Brosset, Carbon **42**, 3189 (2004).
[69]M. Xi and B. E. Bent, J. Phys. Chem. **97**, 4167 (1993).
[70]T. Zecho, A. Horn, J. Biener, and J. Kuppers, Surf. Sci. **397**, 108 (1998).
[71]D. Kolovos-Vellianitis and J. Kuppers, J. Phys. Chem. B **107**, 2559 (2003).
[72]A. Dinger, C. Lutterloh, J. Biener, and J. Kuppers, Surf. Sci. **421**, 17 (1999).
[73]T. Zecho, B. D. Brandner, J. Biener, and J. Kuppers, J. Phys. Chem. B **105**, 6194 (2001).
[74]J. M. Gorham, B. A. Smith, and D. H. Fairbrother, J. Phys. Chem. C **111**, 374 (2007).
[75]E. Vietzke, V. Philipps, K. Flaskamp, P. Koidl, and C. Wild, Surf. Coat. Technol. **47**, 156 (1991).
[76]A. J. Wagner, G. M. Wolfe, and D. H. Fairbrother, J. Chem. Phys. **120**, 3799 (2004).
[77]J. S. Foord, L. C. Hian, and R. B. Jackman, Diamond Relat. Mater. **10**, 710 (2001).
[78]A. Izumi, T. Ueno, Y. Miyazaki, H. Oizumi, and I. Nishiyama, Thin Solid Films **516**, 853 (2008).
[79]See supplementary material at E-JVTBD9-28-072003 for XP spectra, comparable to Fig. 6, showing AO and AH treatment of a film deposited from electron irradiation of $Au(acac)Me_2$ performed on a SiO_2 substrate.